Discussion of possible seismically triggered avalanches after the S1222a Marsquake and S1000a impact event

Lucas A.[1], **Daubar I. J.**[2], **Le Teuff M.**[1], **Perrin C.**[3], **Kawamura T.**[1], **Posiolova L.**[4], **Lognonné P.**[1], **Rodriguez S.**[1], **Giardini D.**[5], **Sainton G.**[1], **Mangeney A.**[1], **McEwen A.**[6]

[1]Université Paris Cité, Institut de physique du globe de Paris, CNRS, F-75005, Paris, France
[2]Brown University, Providence, RI, USA
[3]Nantes Université, Université d'Angers, Le Mans Université, CNRS, UMR 6112, Laboratoire de Planétologie et Géosciences, UAR 3281, Observatoire des Sciences de l'Univers de Nantes Atlantique, Nantes, France
[4]Malin Space Science System, San Diego, CA, USA
[5]ETH, Zurich, Switzerland
[6]U. Arizona, USA

Key Points:

- On May 4, 2022, a major martian seismic event was recorded
- We catalog seismically induced dust avalanches in the area of the estimated epicenter
- We discuss avalanche triggering conditions and derive a possible epicenter location based on avalanche spatial density

Corresponding author: A. Lucas, `lucas@ipgp.fr`

Abstract

Ground motion caused by seismic events detected by the SEIS/InSight seismometer could be expected to trigger dust avalanches on Mars. While we show that impact event S1000a triggered a very large number of dust avalanches, we find only a modest increase in the avalanche rate in the aftermath of the event S1222a . Orbital observations show that the area around the pre-estimated quake location includes some topographic features, including North-South ridge structures and impact craters. We investigate orbital imagery to assess the avalanche rate, and we discuss the influence of the S1222a event on avalanche rates. The S1222a event seems to be a good candidate to explain these increases in the avalanche rate. We re-investigate the epicenter location that would best explain the spatial distribution of the avalanches and discuss possible implications regarding the topographic features in the area.

Plain Language Summary

We discuss the possibility of seismic aftermath on Mars and in particular the fact that a large seismic source can trigger dust avalanches and mass wasting in general. Orbital data show that the source area includes a few steep slopes located mainly at crater walls. The dust cover is also significant in this region, consequently, dust avalanches are common in the area. Large seismic events generate ground acceleration which tends to reduce cohesion, friction, and/or increase tangential strain, all being favorable for triggering mass wasting. Our findings suggest that the S1222a marsquake is a good candidate for explaining an increase in avalanche rate derived from orbital imagery.

1 Introduction

On May 4, 2022, a major seismic event (Kawamura et al., 2023) was recorded by the SEIS instrument (Lognonné et al., 2019) of the InSight mission (Banerdt et al., 2020). It was an unprecedented marsquake in the SEIS recording period with an estimated moment magnitude of M_W^{Ma} 4.7 (InSight Marsquake Service, 2022). In comparison, 95% of events recorded by SEIS since landing in November 2018 have a magnitude below 3.5 (Clinton et al., 2021; BÃűse et al., 2021; Ceylan et al., 2022; Knapmeyer et al., 2023). As for some of the InSight events, a location was estimated with a back-Azimuth (bearing from the event toward InSight) of 101° (96°-112°) and an epicentral distance $\Delta = 37°$ ($\pm 1.6°$) which places the event epicenter at the location of 3.0°S,171.9°E (Kawamura et al., 2023) (green star on Fig. 1). Note that other nearby locations have also been proposed (Panning et al., 2023; Kim et al., 2022)) (Fig. 1). No new impact crater has been reported that could be the source of this event (Fernando et al., 2023). The region shows many topographic features including a few tectonic structures expressed as north-south wrinkle ridges (Knapmeyer et al., 2006) and impact craters (Fig. 1). To the east of this region, the only major structures are Appollinaris Patera, a Noachian volcano (Tanaka et al., 2014) about 200 km in diameter, and a large alluvial fan spanning southwards from the volcano's rim.

From orbital images, dust avalanches (also known as slope streaks) have been identified in this region (orange symbols on Fig. 1). These are known active mass wasting processes occurring on Mars in several contexts (Ferguson & Lucchitta, 1984; Sullivan et al., 2001; Aharonson et al., 2003; Schorghofer et al., 2002, 2007; Schorghofer & King, 2011; Gerstell et al., 2004; Baratoux et al., 2006; Chuang et al., 2007; Bergonio et al., 2013; Heyer et al., 2019, 2020; Valantinas et al., 2021). They appear as relatively dark or bright streaks on steep dust-covered slopes and occur in regions with a high albedo and low to very low thermal inertia (Sullivan et al., 2001; Aharonson et al., 2003). Dust avalanches on Mars typically appear darker than the surrounding terrain. This is likely due to the removal of lighter-colored surface dust by the avalanches. When a slope streak is formed, loose dust and sand on the surface are mobilized and cascade down the slope, exposing
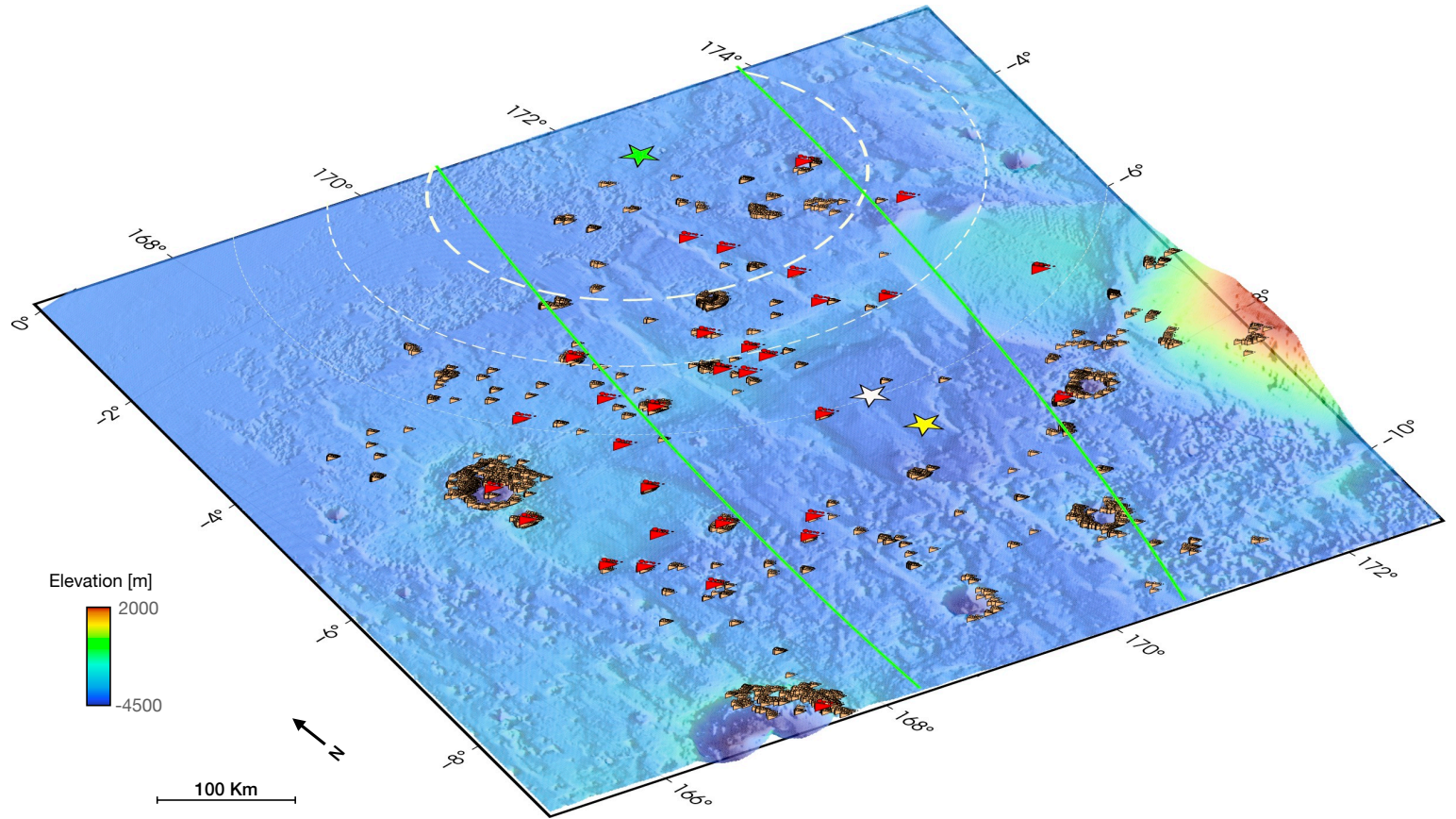
Figure 1. Regional map of dust avalanches near the S1222a event estimated location (green star with associated green ellipse, (Kawamura et al., 2023). The white star is the location estimated by multi-orbit surface waves Panning et al. (2023). The yellow star shows the estimated location according to surface waves (Kim et al., 2022). Dashed white circles represent epicentral distances $\Delta = 2°$, $3°$ and $4°$ from the green star. Orange symbols are all avalanches mapped. Red symbols show where avalanches are observed on post-event images. Basemap is the MOLA elevation map (Smith et al., 2001).

the darker, underlying material (Malin et al., 2007; Dundas, 2020). This material may be darker due to several factors, such as the presence of iron-rich minerals or alteration by weathering processes (Christensen et al., 2001). In addition, the removal of surface dust by the avalanches may expose a rougher, more textured surface, which can scatter and absorb more light, making the streak appear even darker.

Many studies discuss possible triggering conditions and emplacement mechanisms. Purely dry avalanches of fine dust have been explored from the perspective of both observations (Schorghofer et al., 2007; Phillips et al., 2007; Dundas, 2020), and numerical simulations (Lucas, 2010). Spring discharge involving salty groundwater and/or brines in the shallow subsurface has been proposed (Ferris et al., 2002; Miyamoto, 2004; Head et al., 2007; Kreslavsky & Head, 2009; Bhardwaj et al., 2017, 2019). Other possible triggers include wind (Baratoux et al., 2006; Heyer et al., 2019) or seismic activity from impacts or internal forces (Chuang et al., 2007) have been proposed.

While previous studies looked at boulder falls and associated tracks triggered by possible paleo-seismic activity (Roberts et al., 2012; Brown & Roberts, 2019), no previous work could have directly tested the possibility of seismically induced mass wasting on

Mars due to a lack of seismic event records before the InSight mission. In the framework of the recent seismic events S1000a and S1222a, we investigate the effects of the induced ground acceleration aftermaths as a potential triggering mechanism for dust avalanches in the vicinity of the located epicenter. To do so, we conduct regional mapping of the avalanches from pre-event and post-event imagery in order to estimate the effect of the marsquake and impact crater on the rate of avalanches. We take into account possible biases due to the limited number of images, the time span between images, the sub-surface properties through thermal behavior, and the various sensitivities of each camera sensor.

2 Methods

2.1 Orbital data and mapping

As soon as the S1222a event was detected by SEIS and an estimate of the epicenter location was provided, we investigated orbital observations provided by the Context (CTX) and High Resolution Imaging Science Experiment (HiRISE) cameras (Malin et al., 2007; McEwen et al., 2007), both on board the Mars Reconnaissance Orbiter (MRO). Along with MRO imagery, we examine images from the Mars Global Surveyor (MGS)/Mars Orbiter Camera (MOC) and THEMIS-Vis/Odyssey (Fergason et al., 2006). This led to a set of hundreds of images acquired before the seismic event. In addition, we requested new MRO observation over areas where we mapped avalanches inside the uncertainty area (Kawamura et al., 2023) (Fig. 1, Supp. Info text S1). At the time of writing this paper, we have obtained a dozen HiRISE images and thirty new CTX observations, all acquired after the S1222a seismic event. In addition to imagery, we used Digital Terrain Models (DTMs) from both Mars Orbiter Laser Altimeter (MOLA, Smith et al. (2001)) and High Resolution Stereo Camera (HRSC, Neukum and Jaumann (2004)), the geological map from Tanaka et al. (2014) and the thermal inertia map (Christensen et al., 2004) (See Supp. Info text S2), which all provide contextual information. All the data have been combined into a Geographical Information System (GIS) in order to manually map all avalanches in the region of interest (Fig. 1), by two independent people (see Supp Info S1 for details on the imagery processing and mapping). The older observations, provided by both MOC and THEMIS-Vis, were only used for confirming the very low fading rate (Sullivan et al., 2001), being in good agreement with the dust activity reported in this region (Battalio & Wang, 2021).

2.2 Estimates of avalanche rate and statistics

Avalanche rate q is obtained from equation provided in Aharonson et al. (2003):

$$q = 100 \times \frac{\Delta n}{n \Delta t},\tag{1}$$

where n is the total number of avalanches observed in both the two overlapping images, Δn being the newly observed avalanches on the recent image and not in the older image, and Δt being the time span between the two observations in Martian years. This rate q is expressed in % of new events/Martian year (Aharonson et al., 2003). This method has also been used by recent work (Heyer et al., 2019). The time periods between overlapping images in our database range from ~0.3 to almost 7 martian years.

Finally we agglomerate avalanches in the same location (i.e. crater) and hence to compute the avalanche rate in each area where new events can be observed between two overlapping images. As opposed to a squared binning, hexagons are more similar to circles, hence they better translate data aggregation around the bin center. As most areas covered by avalanches in this region are impact craters, this provides a more valuable way to decipher the avalanche coverage.

3 Results and discussion

3.1 Evidence of avalanches triggered after S1000a impact event

Before discussing S1222a event, we investigated S1000a impact event which occurred on September 18 2021, and left a crater over 150 m in diameter at 38.1°N;-79.87°E (Fig. 2). This event was recorded by SEIS and then orbital imagery revealed its actual location. Its magnitude was estimated to be around M_w^{Ma} 4.1, hence about 25 times smaller that S1222a in energy (Ceylan et al., 2022; Posiolova et al., 2022). By analysing post-event HiRISE images, we could map a very large number of avalanches not seen in pre-event imagery. By looking back in time using all available images, including MOC/MGS, we observed that this area was poorly covered by dust avalanches prior to the impact.
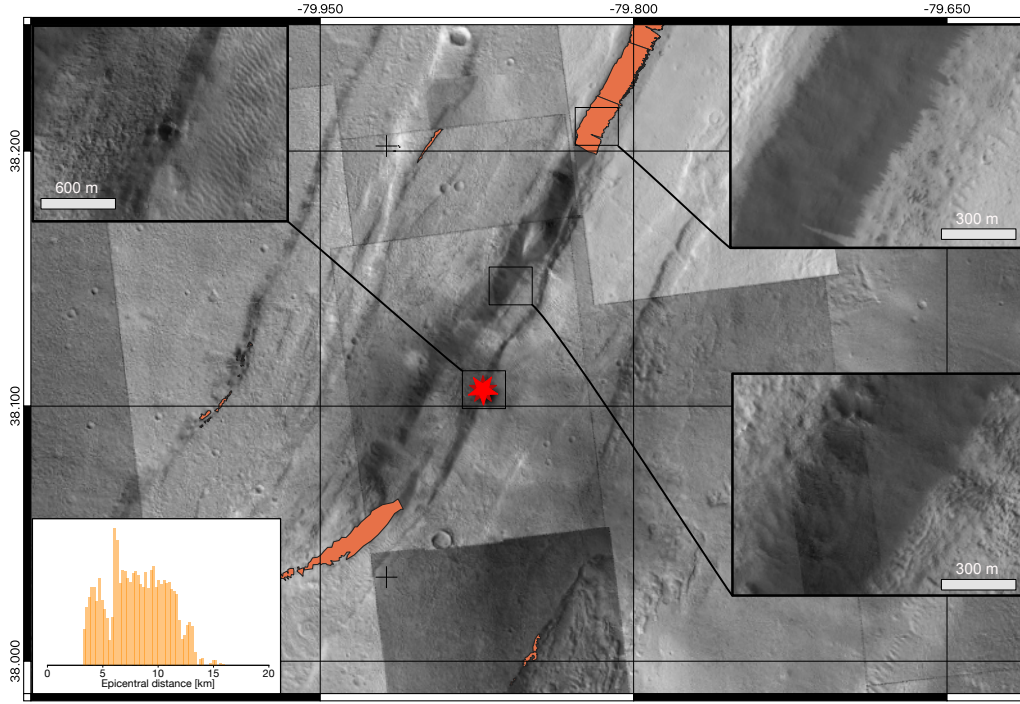

Figure 2. Post-event HiRISE mosaic around the impact location of S1000a event (red star) with associated triggered avalanches (orange areas). Insets show close-up on the crater, the avalanches areas and slopes without new avalanches (from top-left, to bottom-right, respectively). The probability distribution of avalanches with respect to the epicentral distance is shown in the bottom-left inset.

We looked at the the density distribution of the new avalanches (as seen on the post-event images and having the same radiometric signature, hence the same age) as a function of their respective distance to the impact crater (histogram inset in Fig. 2). This distribution follows a bell-shaped curve. As seen on Earth, seismically triggered mass-wasting is absent very close to the epicenter, and increases at farther distances until it decreases again at the farthest distances (e.g., Tatard, 2010; Livio & Ferrario, 2020). Nonetheless, the mechanism here is different. It is very likely that the avalanches are triggered by secondary impacts, and not seismic waves. As an example of a typical scenario, ejecta leaving the primary impact at a velocity v = 200 m.s^{-1}, with a launch angle of θ = 45°, will have a ballistic flight time t_f of 76 sec (i.e., $t_f = 2 \times v \sin\theta/g$), and will land at a distance d_l = 10.78 km (neglecting the air friction, $d_l = v \cos\theta \times t_f$). Hence, the histogram in the inset of figure 2 is similar to the statistical distribution of secondary ejecta impact-

ing the ground. This correlation indicates those secondary impacts are a likely source for the avalanches. Of course, the S1000a event is an ideal case. First of all, we know the position of the epicenter perfectly well, thanks to the orbital imagery revealing the source crater. What's more, the presence of northeast-southwest trending ripples implies the presence of uniformly distributed topographic slopes as moving away from the impact crater, hence the avalanche susceptibility. To summarize, this example shows that an impact with a seismic magnitude M_w^{Ma} 4.1 can trigger a very large number of avalanches on Mars, through secondary impacts. However, the ground accelerations caused by a surface impact and a deep earthquake are not the same. So, in view of our results for the S1000a event, we discuss our results for S1222a in the following sections.

3.2 Evidence of avalanche rate increase in post-marsquake S1222a images

We analyzed all image pairs over the whole area of interest near the S1222a estimated epicenter. We identified 4532 avalanches (orange symbols in Figure 1). More than 200 avalanches were identified on pre-event images (over the 2005–2021 period), and 122 were identified on the post-event CTX images with respect to their 2005–2021 period counterparts respectively. An example is given in Figure 3-a. Note that, while spurious avalanches may have been detected (e.g., yellow symbols in Fig. 3-a), we only took into account the robust observations of new avalanches (e.g., red symbols in Fig. 3-a). For the statistical robustness, we then derived avalanche rates q for each CTX/CTX pair only. When times series were available, we derived avalanche rate chronicles (Fig. 3-b). As exemplified on Fig. 3-b, a strong increase of q is observed after the S1222a event. Indeed, over the whole area of interest (Fig. 1), the pre-event rates (circles in fig. 3-c) lie around 2.6%.MYear^{-1} with a maximum value of 6%.MYear^{-1}, accounting for uncertainties following Aharonson et al. (2003). These values are in agreement with in previous work (Aharonson et al., 2003),and avalanche rates do not differ substantially across the region covered by our study. In contrast, post-event values of q show a significantly different distribution both spatially and in amplitude (Figure 3-c,d). While most rates still fall below 10%, we observe that in 9 places, the rates are >10%, as high as 40% (excluding outlier, Figure 3-d). If we keep only the sub-10% values, the average is the same as that before the seismic event (2.6%/MYear), and there is also no dependence on the epicentral distance. Interestingly, the highest post-event q (>20%) are found at the smallest distances from the epicenter of the S1222a event proposed by Kawamura et al. (2023). When relating the derived avalanche rate q to the epicentral distance Δ with respect to the estimated location from Kawamura et al. (2023), we obtained a slight decreasing trend of q with Δ.

In order to statistically test if there is a significant increase of avalanche rates from image pairs containing post-event observations and accounting the limited number of observations we used a permutation test, also known as bootstrapping (Efron & Tibshirani, 1993; Davison & Hinkley, 1997). A permutation test is a non-parametric approach that doesn't rely on specific assumptions about the distribution of the data. First, we calculate the avalanches rate for each CTX/CTX pair for pre-event and post-event observation. We compute their mean difference (i.e., the observed statistics). Then, we combine the pre-event and post-event rates into a single pool, disregarding their original times. We randomly shuffle the data of the pooled data to create new randomized groups by maintaining the original sizes of both groups. We calculate the permuted test statistic (i.e., compute the rate of avalanches for the permuted data). We iterate the permutation process a million times to generate a distribution of test statistics under the assumption of no influence from the marsquake. Then, we compare the observed statistics to the 95% confidence interval test statistics obtained from the bootstrapping. When accounting for all CTX observations, the avalanche rates derived from post-event images is above 95% of the bootstrap statistic distribution. Note that this area contains places that may be too far away from the epicentre to be affected by the marsquake. When only accounting for the rates above 6%.MYear^{-1}, the post marsquake rates fall above the 99.98% of confidence (See Supp

Info Text S3). Finally we also verified that temporal sampling of the orbital images (Δt)
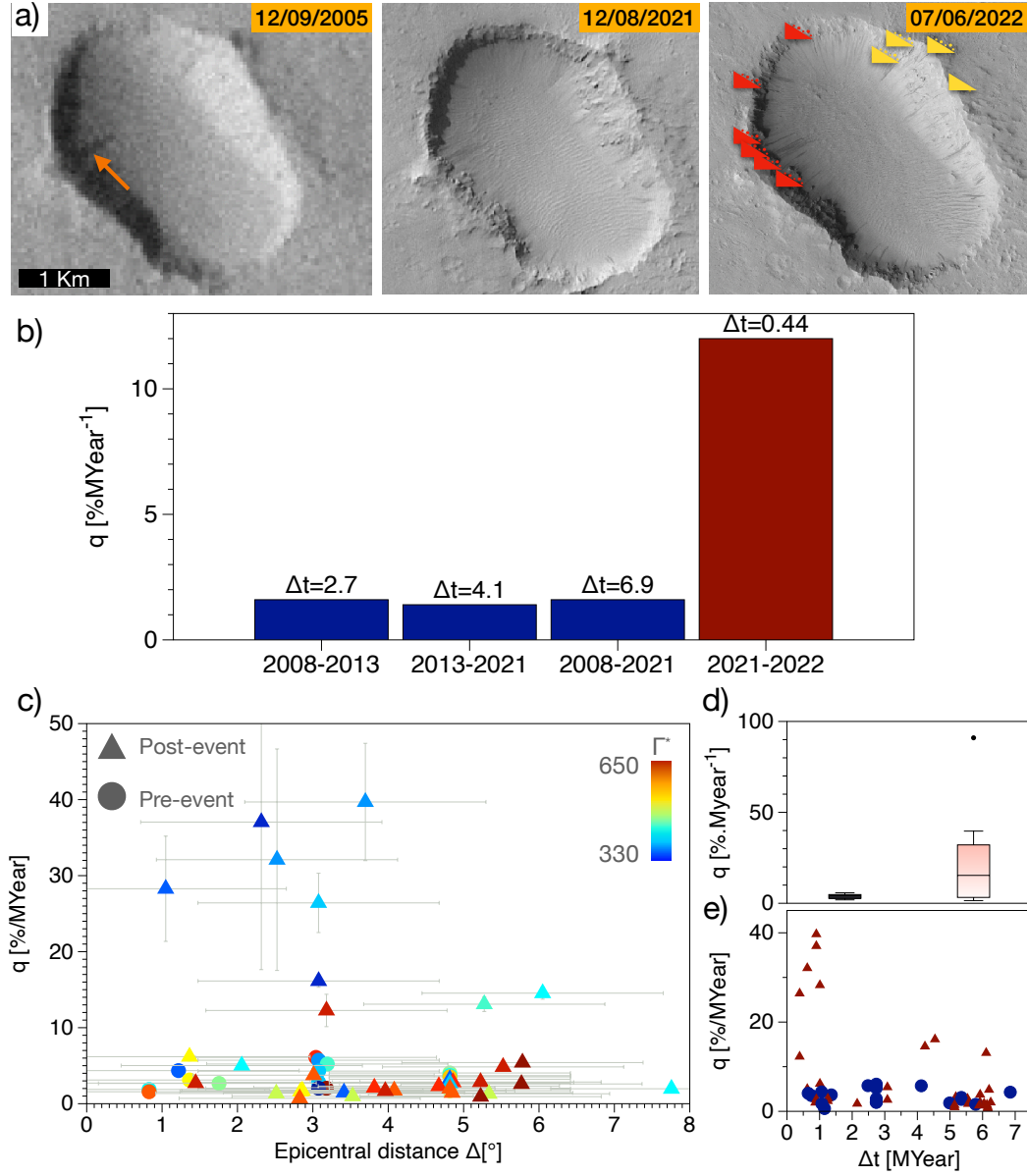does not affect the avalanche rate estimates (Fig. 3-e).

Figure 3. a) Image times series with THEMIS-Vis image V1768100 (17m/pixel) taken in 2005, CTX image N21_070520_1744_XI_05S189W (6m/pixel) taken 8 months before S1222a, and an HiRISE image (downsampled to 5m/pixel) ESP_074357_1745 taken a few weeks after the marsquake. New avalanches marked with the red symbols. Additional spurious avalanches are indicated with the yellow symbols, b) time series of avalanche rate q over the 2008-2022 period. c) Avalanche rate q as a function of the epicentral distance Δ (with respect to the green star of Fig. 1) for CTX/CTX image pairs. Symbols are associated to pre-event (circles) or post-event (triangles). Color scales with the apparent thermal inertia (Γ*, see Supp Info text S2). d) Box plot of avalanche rates for pre-event pairs (black) and pre/post-event pairs (red). e) Avalanche rate q as a function of timespan Δt. Note that some symbols can overlap each other on both plots.

3.3 Discussion on the apparent thermal inertia and the triggered avalanches

Subsurface properties at shallow depth can be derived through thermal inertia, which is related to how solar energy is absorbed and the resulting heat propagates within the subsurface and re-emitted. Hence thermal inertia strongly correlates with the material properties as $\Gamma \equiv \sqrt{\kappa_e(1-p)\rho C(T)}$, where κ_e is the effective thermal conductivity, p the porosity, ρ the density and $C(T)$ specific heat capacity. Thus a low thermal inertia could be an indication of either high porosity, low density, small grain size, or a combination of those parameters. As previously shown and discussed, dust avalanches occur on steep slopes (see Supp. Info Fig. S2) and mostly over low thermal inertia areas (Sullivan et al., 2001; Aharonson et al., 2003). Note that value of the thermal inertia is derived from models and assumptions after (Christensen et al., 2004). As strong variations are obtained between orbits, we derive an apparent value, hereafter named Γ^*. A discussion on how we extract this apparent value is detailed in the supplementary information (see Supp. Info text S2). Because avalanches form on steep slopes, they are actually associated with higher apparent thermal inertia than that of the surrounding terrains. The latter probably being covered with a thicker dust mantle. Considering apparent thermal inertia over the pixels at avalanches scarp (Γ^*), the areas with the lowest values are experiencing the largest increases in the avalanche rate (Fig. 3-c). When $\Gamma^* \gg 450$ S.I., the post-event rate is not higher than the pre-event period. In contrast, we only observed an increase of q, when $\Gamma^* < 450$ S.I. We can conclude that post-event avalanche susceptibility is controlled by scarp locations associated with steep slopes and low apparent thermal inertia, corresponding to the most unconsolidated terrains, and/or fine granular material.

3.4 Discussion on the epicentral distance and possible sources of the quake

Although the epicentral distance is far from being the only parameter that controls the avalanche rates, it remains an important control factor. The reason is that the transition between a static state and a flowing state is modelled by introducing a threshold allowing the material to flow. This has been shown to quantitatively capture debris and rock avalanche morphodynamics on Mars (Lucas, 2010; Lucas & Mangeney, 2007; Lucas et al., 2011, 2014) (see Supp. Info Text. S4). Nonetheless, local geology, fractures, aftershocks and historical events will have a significant effect on the aftermaths of an earthquake by leading the slopes close to failure (Tatard, 2010; Livio & Ferrario, 2020; Chen et al., 2020; Rosser et al., 2021; Lombardo & Tanyas, 2022). Taking into account all these considerations, the rate would not be expected to be controlled only by epicentral distance. However, our constraints on the characteristics of the marsquake are weak, especially in terms of depth, focal mechanisms, and therefore the resulting ground acceleration. Our knowledge on the geological heterogeneity is also poorly constrained. Also, compared to terrestrial standards, this marsquake remains a small event. Nonetheless, small seismic events have shown to significantly increase the rate of landslides on Earth (Martino et al., 2022). Indeed, recent studies show that even very small amplitude seismicity may trigger instabilities on metastable slopes (Bontemps et al., 2020; Durand et al., Minor revision).

Nonetheless, under the hypothesis that event S1222a did trigger avalanches, we considered the empirical model proposed by Livio and Ferrario (2020) which relates the distribution of triggered avalanches N_{ava} with the epicentral distance Δ:

$$G(\mathbf{m}) = N_{ava} = a \exp\left[-\left(\frac{\Delta - b}{c}\right)^2\right], \tag{2}$$

where a is the amplitude of the distribution, b the distance of the peak amplitude and c the width of the distribution. While we do not have images just before and just after the event, we derived an estimation of the number of triggered avalanches from this relationship:

$$N_{ava} = \Delta n - \bar{q} \times n\Delta t/100, \tag{3}$$

where $\bar{q}$ is the long-term avalanche rate (i.e., we conservatively considered $6\%\mathrm{MYear}^{-1}$). Because the avalanche susceptibility is not evenly distributed (i.e., steep slopes only located inside impact craters, non-homogeneous surface/sub-surface properties), we only consider observations that meet the following criteria: $\Gamma^* < 580$ SI, and $\Delta t < 1.5$ MYear, to only account for the lowest thermal inertia (see Fig. 3) and the smallest time span between images to reduce biases. Then, we used a Monte Carlo method to invert the most probable epicenter location using a maximum likelihood function with a Laplacian distribution of errors (Mosegaard & Tarantola, 1995) (See Supp Info Text S5). The resulting probability distribution of the epicenter under all of these considerations is given in Figure 4. It is situated in between the locations obtained from both body and surface waves analysis respectively (Kawamura et al., 2023; Panning et al., 2023; Kim et al., 2022), then included in the uncertainty ellipses of epicentral locations (green contours in Fig. 4).

This distribution can lead us to two different interpretations regarding the source mechanism of the quake, mainly related to internal tectonic activity. A first hypothesis would be based on the fact that our distribution is slightly shifted toward the East from the wrinkle ridges, on the flanks of Apollinaris Patera. It is now well supported that Mars still hosts remnant volcano-tectonic activity, especially along Cerberus Fossae (Giardini et al., 2020; Horvath et al., 2021; Perrin et al., 2022; Stähler et al., 2022), possibly due to the presence of a plume (Broquet & Andrews-Hanna, 2022), and associated with normal slip motion (Brinkman et al., 2021; Jacob et al., 2022). While the moment tensor analysis of the S1222a event can give very different slip motions, NNW-SSE normal faulting is a possible solution (Maguire et al., 2023), highlighting a possible activity of Apollinaris Patera at depth. However, unlike Cerberus Fossae, Apollinaris Patera is an old Noachian volcano, thus it seems unlikely that remnant volcanic activity would be present at shallow depth. A second hypothesis would be related to the 450 km long wrinkle ridge, trending NNE-SSW, and cross-cutting the Hesperian terrains between the two epicentral locations (black lines in figure 4). The probability distribution of the epicenter inverted from the avalanche rate is about 30 to 60 km East of this major structure. The shape of the topographic profile across the ridge is an asymmetric arch-ridge, with a steep slope facing West and a shallow slope facing East (Fig. 1), which would imply a main East-dipping thrust at depth (Andrews-Hanna, 2020). Assuming a fault dip of $34°$ to $42°$ for arch-ridges (Andrews-Hanna, 2020), a probability distribution situated about 30 to 60 km East of the wrinkle ridge would lead to a hypocentral depth ranging from 20 to 54 km. This range of depth is in agreement with the best solutions found by Maguire et al., 2023. They also present mainly reverse slip motions striking E-W to NW-SE, which is not optimally oriented with the overall wrinkle ridge observed from orbital imagery. However, local large variations in fault strikes are possible along a wrinkle ridge. Note that the wrinkle ridges are cross-cutting a large E-W bulge situated at about -5° latitude, connecting the flanks of Apollinaris Patera and a large crater in the west (Fig. 1). This bulge presents hundreds of meters of difference in elevation and slight apparent thermal inertia anomalies that could indicate a bedrock affected by an old tectonic structure. Interestingly, the bulge's azimuth is aligned with our probability distribution of the epicenter. More work would be needed to understand the origin of this structure and a possible link with the source of the marsquake.

It should also be noted that source locations obtained from other methods such as surface waves or coda characteristics give different locations (Kim et al., 2022; Panning et al., 2023; Menina et al., 2023). Both studies using surface waves predict source locations more towards the south as shown in 4. This is due to different back azimuth they obtained for surface waves compared from that described in (Kawamura et al., 2023) using body waves. Panning et al. (2023) also discusses the possibility that the source location could be in the southern hemisphere. Interestingly, Menina et al. (2023) conclude that they need a thick (60km) diffusive layer to explain the coda shape of S1222a. This could imply that either the source location could be in the highlands of the southern hemisphere
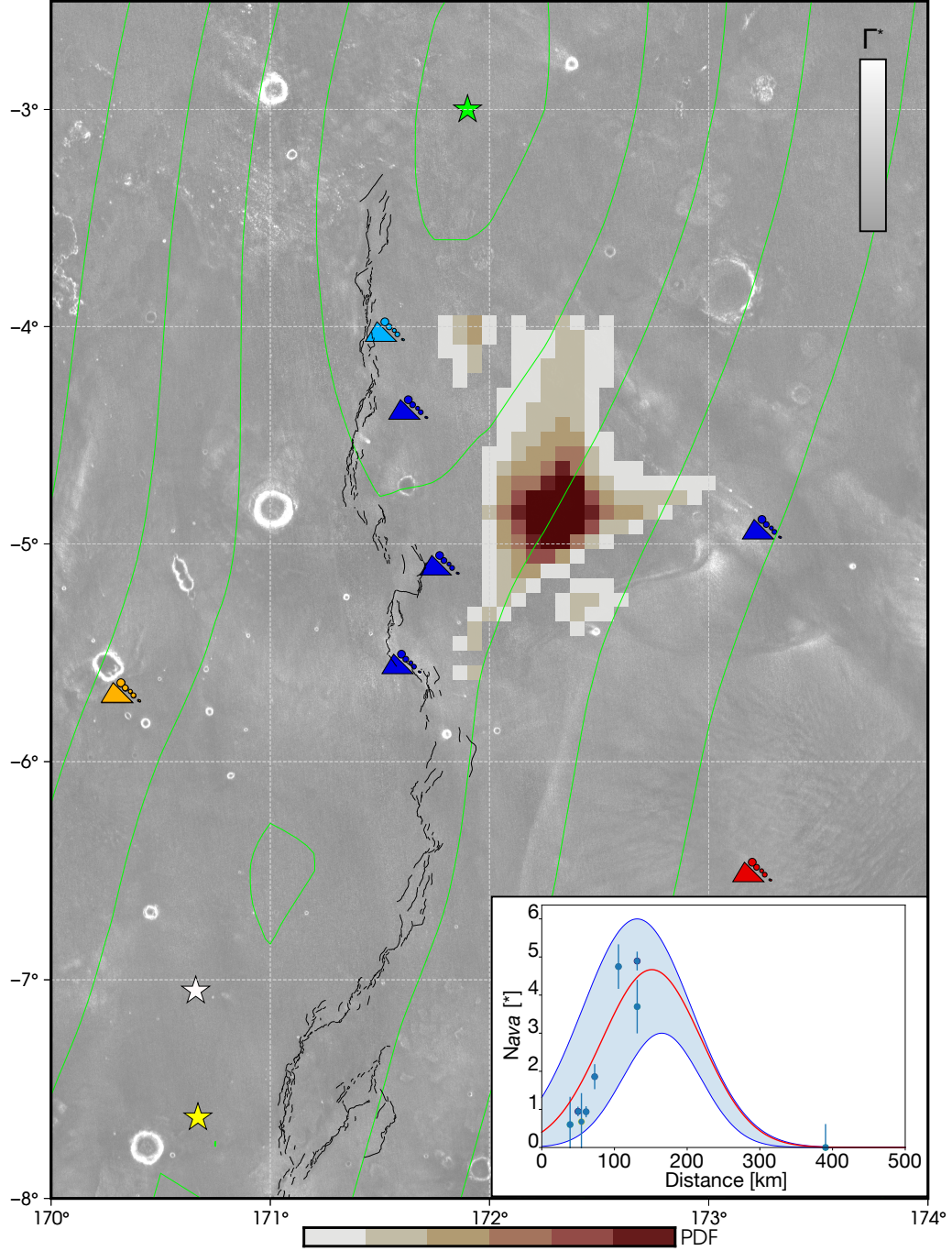
Figure 4. Probability distribution of the epicenter inverted from avalanche observations (reddish colormap). Symbols show number of avalanches N_{ava} due to the S1222a event. The green star (upper center) is the maximum peak of the estimated epicenter and its uncertainty ellipses (green contours) obtained from body waves (Kawamura et al., 2023), the white star, the location estimated from multi-orbit surface waves (Panning et al., 2023), and the yellow star is the estimated epicenter derived from the surface waves (Kim et al., 2022). Black lines are detailed surface traces of the main wrinkle ridge in the vicinity of the epicentral area. Background map is the thermal inertia Γ^*. (Inset) Expected avalanche density distribution with confidence interval from Monte Carlo inversion using equation 2 with respect to the number of avalanche derived from equation 3.

(Wieczorek et al., 2022), or that thermal anomalies at depth are present in the Appollinaris area.

Our work leads us to propose that the source of the quake is likely due to thermal contraction due to Mars' cooling through time. The peak of thermal contraction and wrinkle ridge formation occurred during the early Hesperian and decreased progressively until now (Watters, 1993). Even if the wrinkle ridge in figure 4 is well expressed in morphology, its surface trace ends to the north, near the transition between Hesperian and Amazonian terrains (Tanaka et al., 2014). This indicates that the ridge has not been active in recent times. However, thermal contraction is still ongoing on Mars and might re-activate local mechanical weaknesses in the martian crust, such as wrinkle ridges, over larger recurrence time periods. If such activity is real, microseismicity should be associated with it.

4 Conclusions

In our investigation of surface features around both the S1000a and the S1222a seismic events, we take advantage of the MRO orbital data acquired in the vicinity of the estimated location to estimate the associated avalanche rate. In the case of the S1000a impact event, the very large amount of avalanches on post-event orbital imagery strongly support its indirect aftermaths, likely through secondary impacts. As such, this is likely be discussed more thoroughly in a following paper which will provide that distribution of secondaries by ballistic recomposition. For the seismic event S1222a, things are less obvious and requested care investigation. First, we retrieve long-term dust avalanche rates, being similar to both global estimates from Aharonson et al. (2003) as well as in the vicinity of Olympus Mons from Heyer et al. (2019). Those pre-event rates range between 1 and $6\%.\text{MYears}^{-1}$ new events. We verified that no biases were introduced either in terms of location, apparent thermal inertia, or the time span between CTX image pairs that were used to derive those avalanche rates. We find a significant increase in the avalanche rates (up to $40\%.\text{MYear}^{-1}$ compared to the pre-event $\sim2.6\%.\text{MYear}^{-1}$ in average, this latter being in agreement with previous estimates Aharonson et al. (2003)) in locations close to the estimated epicenter (Kawamura et al. (2023); Panning et al. (2023); Kim et al. (2022)), where the apparent thermal inertia is relatively low. Consequently, we propose that the S1222a marsquake may be a good candidate for explaining the modest increased avalanche rate derived from orbital imagery. Assuming a radial ground acceleration, we estimate the most probable marsquake epicenter that could explain the observed avalanche rate when accounting for the apparent thermal inertia threshold.

Finally, we discuss the implications of our inverted location with respect to the presence of a volcanic edifice as well as a North-South wrinkle ridge structure located close to the peak of the probability distribution function. This work shows that current seismic activity on Mars is able to initiate mass wasting processes such as dust avalanches, also known as slope streaks. This gives the opportunity to explore places where avalanches are observed and where other seismic events have been located thanks to the InSight mission. In the light of our results, it is likely that avalanche rates should increase in regions on Mars where episodic/sporadic seismic sources would lead to ground deformation. This approach can be used for future analyses of other seismic events. Their visible aftermaths, such as avalanches, could reveal substantial constraints on the epicenter locations. In a more general way, we show that avalanches can be used to document fast processes, like impacts (which are discrete surface perturbations) or quakes (which are more continuous).

6 Open Research

The orbital data are available online: HRSC are available at ESA's Planetary Science Archive (`https://www.cosmos.esa.int/web/psa/mars-express`). THEMIS data are available at Arizona State University's repository (`https://themis.asu.edu`). MOC images are available at the PDS Imaging Node (`https://pds-imaging.jpl.nasa.gov/data/mgs-m-moc-na_wa-2-sdp-l0-v1.0/`). MOLA data are available at the PDS Geosciences Node (`https://pds-geosciences.wustl.edu/missions/mgs/mola.html`). HiRISE data, including the post-event images, are available at the University of Arizona's dedicated website (`https://www.uahirise.org`). CTX image are available at the Imaging PDS Node (`https://pds-imaging.jpl.nasa.gov/data/mro/mars_reconnaissance_orbiter/ctx/`). The post-event CTX images will be posted on the NASA PDS by MSSS by the time of publication. Meanwhile, referee's can have access to the mosaic at `https://www.dropbox.com/sh/u1cykaotwxvi7ga/AAAsDcqw4FrkGDqjb4HTFmjka?dl=0`. The avalanche catalogue is available on Zenodo (doi:10.5281/zenodo.7679315). The InSight seismic event catalogue version 9 (InSight Marsquake Service, 2022) and waveform data (InSight Mars SEIS Data Service, 2019a,b) are available from the IPGP Datacenter and IRIS-DMC, as are previous catalogue versions. Seismic waveforms are also available from NASA PDS. The crustal thickness grid is available on Zenodo (doi:10.5281/zenodo.6477509).

References

Aharonson, O., Schorghofer, N., & Gerstell, M. F. (2003). Slope streak formation and dust deposition rates on Mars: Martian slope streak formation rates. *Journal of Geophysical Research: Planets*, *108*(E12). Retrieved 2022-07-14, from `http://doi.wiley.com/10.1029/2003JE002123` doi: 10.1029/2003JE002123

Andrews-Hanna, J. C. (2020). The tectonic architecture of wrinkle ridges on Mars. *Icarus*, *351*(October 2019), 113937. Retrieved from `https://doi.org/10.1016/j.icarus.2020.113937` doi: 10.1016/j.icarus.2020.113937

Banerdt, W. B., Smrekar, S. E., Banfield, D., Giardini, D., Golombek, M., Johnson, C. L., ... Wieczorek, M. (2020, Mar 01). Initial results from the insight mission on mars. *Nature Geoscience*, *13*(3), 183-189.

Baratoux, D., Mangold, N., Forget, F., Cord, A., Pinet, P., Daydou, Y., ... HRSC CO-Investigator Team (2006). The role of the wind-transported dust in slope streaks activity: Evidence from the HRSC data. *Icarus*, *183*(1), 30-45. doi: 10.1016/j.icarus.2006.01.023

Battalio, M., & Wang, H. (2021). The Mars Dust Activity Database (MDAD): A comprehensive statistical study of dust storm sequences. *Icarus*, *354*, 114059. Retrieved 2022-07-14, from `https://linkinghub.elsevier.com/retrieve/pii/S001910352030405X` doi: 10.1016/j.icarus.2020.114059

Bergonio, J. R., Rottas, K. M., & Schorghofer, N. (2013). Properties of martian slope streak populations. *Icarus*, *225*(1), 194-199. Retrieved from `https://www.sciencedirect.com/science/article/pii/S0019103513001395` doi: https://doi.org/10.1016/j.icarus.2013.03.023

Bhardwaj, A., Sam, L., Martín-Torres, F. J., Zorzano, M.-P., & Fonseca, R. M. (2017). Martian slope streaks as plausible indicators of transient water activity. *Scientific Reports*, *7*(1), 7074. Retrieved from `https://doi.org/10.1038/s41598-017-07453-9` doi: 10.1038/s41598-017-07453-9

Bhardwaj, A., Sam, L., MartĂŋn-Torres, F. J., & Zorzano, M.-P. (2019). Are slope streaks

indicative of global-scale aqueous processes on contemporary mars? *Reviews of Geophysics*, *57*(1), 48-77. doi: https://doi.org/10.1029/2018RG000617

Bontemps, N., Lacroix, P., Larose, E., Jara, J., & Taipe, E. (2020). Rain and small earthquakes maintain a slow-moving landslide in a persistent critical state. *Nature Communications*, *11*(1), 780.

Brinkman, N., StÃđhler, S. C., Giardini, D., Schmelzbach, C., Khan, A., Jacob, A., . . . Banerdt, W. B. (2021). First focal mechanisms of marsquakes. *Journal of Geophysical Research: Planets*. Retrieved from `https://agupubs.onlinelibrary .wiley.com/doi/abs/10.1029/2020JE006546` doi: https://doi.org/10.1029/ 2020JE006546

Broquet, A., & Andrews-Hanna, J. C. (2022). Geophysical evidence for an active mantle plume underneath Elysium Planitia on Mars. *Nature Astronomy*. doi: 10.1038/s41550 -022-01836-3

Brown, J., & Roberts, G. (2019). Possible evidence for variation in magnitude for marsquakes from fallen boulder populations, Grjota Valles, Mars. *J. Geophys. Res. Planets*, *124*(3), 801-812. doi: 10.1029/2018JE005622

BÃűse, M., StÃđhler, S. C., Deichmann, N., Giardini, D., Clinton, J., LognonnÃľ, P., . . . Banerdt, W. B. (2021, 06). Magnitude Scales for Marsquakes Calibrated from InSight Data. *Bulletin of the Seismological Society of America*, *111*(6), 3003-3015.

Ceylan, S., Clinton, J. F., Giardini, D., StÃđhler, S. C., Horleston, A., Kawamura, T., . . . Banerdt, W. B. (2022). The marsquake catalogue from insight, sols 0âĂŞ1011. *Physics of the Earth and Planetary Interiors*, *333*, 106943.

Chen, X.-l., Shan, X., Wang, M.-m., Liu, C.-g., & Han, N.-n. (2020, 03). Distribution pattern of coseismic landslides triggered by the 2017 jiuzhaigou ms 7.0 earthquake of china: Control of seismic landslide susceptibility. *ISPRS International Journal of Geo-Information*, *9*, 198. doi: 10.3390/ijgi9040198

Christensen, P. R., Bandfield, J. L., Hamilton, V. E., Ruff, S. W., Kieffer, H. H., Titus, T. N., . . . Greenfield, M. (2001). Mars global surveyor thermal emission spectrometer experiment: Investigation description and surface science results. *Journal of Geophysical Research: Planets*, *106*(E10), 23823-23871.

Christensen, P. R., Jakosky, B. M., Kieffer, H. H., Malin, M. C., Jr, H. Y. M., Nealson, K., . . . Ravine, M. (2004). The thermal emission imaging system (themis) for the mars 2001 odyssey mission. In C. T. Russell (Ed.), *2001 mars odyssey* (pp. 85–130). Dordrecht: Springer Netherlands.

Chuang, F. C., Beyer, R. A., McEwen, A. S., & Thomson, B. J. (2007). HiRISE observations of slope streaks on mars. *Geophysical Research Letters*, *34*(20). Retrieved from `https://agupubs.onlinelibrary.wiley.com/doi/abs/10.1029/ 2007GL031111` doi: https://doi.org/10.1029/2007GL031111

Clinton, J. F., Ceylan, S., van Driel, M., Giardini, D., StÃđhler, S. C., BÃűse, M., . . . Stott, A. E. (2021). The marsquake catalogue from insight, sols 0âĂŞ478. *Physics of the Earth and Planetary Interiors*, *310*, 106595.

Davison, A. C., & Hinkley, D. V. (1997). *Bootstrap methods and their application*. Cambridge University Press.

Dundas, C. M. (2020). Geomorphological evidence for a dry dust avalanche origin of slope streaks on mars. *Nature Geoscience*, *13*(7), 473–476. Retrieved from `https://doi .org/10.1038/s41561-020-0598-x` doi: 10.1038/s41561-020-0598-x

Durand, V., Mangeney, A., Bernard, P., Bonilla, L. F., Satriano, C., Jia, X., . . . Hibert, C. (Minor revision). The competing role of seismicity and rainfall in slope destabilization: rockfalls triggered on a metastable volcanic edifice. *Science Advances*.

Efron, B., & Tibshirani, R. J. (1993). *An introduction to the bootstrap*. CRC Press.

Fergason, R. L., Christensen, P. R., & Kieffer, H. H. (2006, dec). High-resolution thermal inertia derived from the Thermal Emission Imaging System (THEMIS): Thermal model and applications. *Journal of Geophysical Research: Planets*, *111*(E12), n/a–n/a. Retrieved from `http://doi.wiley.com/10.1029/2006JE002735` doi: 10.1029/2006JE002735

Ferguson, H. M., & Lucchitta, B. K. (1984). *Dark streaks on talus slopes, Mars.* In NASA. Washington Rept. of Planetary Geol. Programs p 188-190 (SEE N84-23431 13-91).

Fernando, B., Daubar, I., Grindrod, P., Stott, A., Ateqi, A. A., Atri, D., ... Banerdt, W. (2023). Searching for transients or a fresh crater at the origin of insight's largest marsquake. *54th Lunar and Planetary Science Conference*, *2806*.

Ferris, J. C., Dohm, J. M., Baker, V. R., & Maddock III, T. (2002). Dark slope streaks on mars: Are aqueous processes involved? *Geophysical Research Letters*, *29*(10), 128-1-128-4. Retrieved from `https://agupubs.onlinelibrary.wiley.com/doi/abs/10.1029/2002GL014936` doi: https://doi.org/10.1029/2002GL014936

Gerstell, M. F., Aharonson, O., & Schorghofer, N. (2004). A distinct class of avalanche scars on Mars. *Icarus*, *168*(1), 122–130. Retrieved 2022-07-14, from `https://linkinghub.elsevier.com/retrieve/pii/S0019103503003907` doi: 10.1016/j.icarus.2003.11.005

Giardini, D., Lognonné, P., Banerdt, W., Pike, W., Christensen, U., Ceylan, S., ... Yana., C. (2020). The Seismicity of Mars. *Nature Geoscience*, *13*(3), 205–212. doi: http://doi.org/10.1038/s41561-020-0539-8

Head, J. W., Marchant, D. R., Dickson, J. L., Levy, J. S., & Morgan, G. A. (2007, March). Slope Streaks in the Antarctic Dry Valleys: Characteristics, Candidate Formation Mechanisms, and Implications for Slope Streak Formation in the Martian Environment. In *38th annual lunar and planetary science conference* (p. 1935).

Heyer, T., Kreslavsky, M., Hiesinger, H., Reiss, D., Bernhardt, H., & Jaumann, R. (2019). Seasonal formation rates of martian slope streaks. *Icarus*, *323*, 76–86. Retrieved 2022-07-14, from `https://linkinghub.elsevier.com/retrieve/pii/S0019103518306857` doi: 10.1016/j.icarus.2019.01.010

Heyer, T., Raack, J., Hiesinger, H., & Jaumann, R. (2020). Dust devil triggering of slope streaks on mars. *Icarus*, *351*, 113951. Retrieved from `https://www.sciencedirect.com/science/article/pii/S0019103520303249` doi: https://doi.org/10.1016/j.icarus.2020.113951

Horvath, D. G., Moitra, P., Hamilton, C. W., Craddock, R. A., & Andrews-Hanna, J. C. (2021, September). Evidence for geologically recent explosive volcanism in Elysium Planitia, Mars. *Icarus*, *365*, 114499. doi: 10.1016/j.icarus.2021.114499

InSight Marsquake Service. (2022). *Mars seismic catalogue, insight mission; v12 2022-10-01.* ETHZ, IPGP, JPL, ICL, Univ. Bristol. Retrieved from `https://www.insight.ethz.ch/seismicity/catalog/v12` doi: 10.12686/a18

Jacob, A., Plasman, M., Perrin, C., Fuji, N., Lognonnår, P., Xu, Z., ... Banerdt, W. (2022). Seismic sources of insight marsquakes and seismotectonic context of elysium planitia, mars. *Tectonophysics*, *837*, 229434. Retrieved from `https://www.sciencedirect.com/science/article/pii/S0040195122002281` doi: https://doi.org/10.1016/j.tecto.2022.229434

Kawamura, T., Clinton, J., Zenhäusern, G., Ceylan, S., Horleston, A., Dahmen, N., ... Banerdt, W. (2023). S1222a - the largest Marsquake detected by InSight. *Geophysical Research Letters*. doi: 10.1029/2022GL101543

Kim, D., StÃďhler, S. C., Ceylan, S., Lekic, V., Maguire, R., ZenhÃďusern, G., ... Banerdt, W. B. (2022). Structure along the martian dichotomy constrained by rayleigh and love waves and their overtones. *Geophysical Research Letters*, e2022GL101666.

Knapmeyer, M., Oberst, J., Hauber, E., Wählisch, M., Deuchler, C., & Wagner, R. (2006). Working models for spatial distribution and level of Mars' seismicity. *J. Geophys. Res. E Planets*, *111*(11), 1–23. doi: 10.1029/2006JE002708

Knapmeyer, M., StÃďhler, S., Plesa, A.-C., Ceylan, S., Charalambous, C., Clinton, J., ... Banerdt, W. B. (2023). The global seismic moment rate of mars after event s1222a. *Geophysical Research Letters*, *50*(7), e2022GL102296.

Kreslavsky, M. A., & Head, J. W. (2009). Slope streaks on Mars: A new "wet" mechanism. *Icarus*, *201*(2), 517–527. Retrieved 2022-07-14, from `https://linkinghub.elsevier.com/retrieve/pii/S0019103509000608` doi: 10.1016/j.icarus.2009.01.026

Livio, F., & Ferrario, M. F. (2020). Assessment of attenuation regressions for earthquake-triggered landslides in the italian apennines: insights from recent and historical events. *Landslides*, *17*(12), 2825-2836.

Lognonné, P., Banerdt, W. B., Giardini, D., Pike, W. T., Christensen, U., Laudet, P., . . . Wookey, J. (2019, feb). SEIS: Insight's Seismic Experiment for Internal Structure of Mars. *Space Science Reviews*, *215*(1), 12. Retrieved from `http://dx.doi.org/10.1007/s11214-018-0574-6http://link.springer.com/10.1007/s11214-018-0574-6` doi: 10.1007/s11214-018-0574-6

Lombardo, L., & Tanyas, H. (2022). From scenario-based seismic hazard to scenario-based landslide hazard: fast-forwarding to the future via statistical simulations. *Stoch Environ Res Risk Assess*, *36*, 2229–2242.

Lucas, A. (2010). *Dynamique des instabilités gravitaires par modélisation et télédétection: Applications aux exemples martiens* (Theses, Institut de physique du globe de paris - IPGP). Retrieved from `https://tel.archives-ouvertes.fr/tel-00503212`

Lucas, A., & Mangeney, A. (2007). Mobility and topographic effects for large valles marineris landslides on mars. *Geophysical Research Letters*, *34*(10).

Lucas, A., Mangeney, A., & Ampuero, J. P. (2014). Frictional velocity-weakening in landslides on earth and on other planetary bodies. *Nature Communications*, *5*(1), 3417.

Lucas, A., Mangeney, A., MÃĺge, D., & Bouchut, F. (2011). Influence of the scar geometry on landslide dynamics and deposits: Application to martian landslides. *Journal of Geophysical Research: Planets*, *116*(E10).

Maguire, R. R., Lekić, V., Schmerr, N. C., Kim, D., Li, J., Beghein, C., . . . Bruce Banerdt, W. (2023). Moment Tensor Estimation of Event S1222a and Implications for Tectonics Near the Dichotomy Boundary in Southern ELysium Planitia Mars. *Journal of Geophysical Research E: Planets*, *submitted*.

Malin, M. C., Bell, J. F., Cantor, B. A., Caplinger, M. A., Calvin, W. M., Clancy, R. T., . . . Wolff, M. J. (2007, may). Context Camera Investigation on board the Mars Reconnaissance Orbiter. *Journal of Geophysical Research*, *112*(E5), E05S04. Retrieved from `http://doi.wiley.com/10.1029/2006JE002808` doi: 10.1029/2006JE002808

Martino, S., Fiorucci, M., Marmoni, G. M., Casaburi, L., Antonielli, B., & Mazzanti, P. (2022). Increase in landslide activity after a low-magnitude earthquake as inferred from dinsar interferometry. *Scientific Reports*, *12*(1), 2686.

McEwen, A. S., Eliason, E. M., Bergstrom, J. W., Bridges, N. T., Hansen, C. J., Delamere, W. A., . . . Weitz, C. M. (2007, may). Mars Reconnaissance Orbiter's High Resolution Imaging Science Experiment (HiRISE). *Journal of Geophysical Research*, *112*(E5), E05S02. Retrieved from `http://doi.wiley.com/10.1029/2005JE002605` doi: 10.1029/2005JE002605

Menina, S., Margerin, L., Kawamura, T., Heller, G., Drilleau, M., Xu, Z., . . . Banerdt, W. B. (2023). Stratification of heterogeneity in the lithosphere of mars from envelope modeling of event s1222a and near impacts: Interpretation and implications for very-high-frequency events. *Geophysical Research Letters*, *50*(7), e2023GL103202.

Miyamoto, H. (2004). Fluid dynamical implications of anastomosing slope streaks on Mars. *Journal of Geophysical Research*, *109*(E6), E06008. Retrieved 2022-07-14, from `http://doi.wiley.com/10.1029/2003JE002234` doi: 10.1029/2003JE002234

Mosegaard, K., & Tarantola, A. (1995). Monte carlo sampling of solutions to inverse problems. *Journal of Geophysical Research: Solid Earth*, *100*(B7), 12431-12447. doi: https://doi.org/10.1029/94JB03097

Neukum, G., & Jaumann, R. (2004). The high resolution stereo camera of mars express. *ESA Special Publication*, *1240*, 1–19.

Panning, M. P., Banerdt, W. B., Beghein, C., Carrasco, S., Ceylan, S., Clinton, J. F., . . . ZenhÃđusern, G. (2023). Locating the largest event observed on mars with multi-orbit surface waves. *Geophysical Research Letters*, *50*(1), e2022GL101270.

Perrin, C., Jacob, A., Lucas, A., Myhill, R., Hauber, E., Batov, A., . . . Fuji, N. (2022). Geometry and segmentation of cerberus fossae, mars: Implications for marsquake properties. *J. Geophys. Res.: Planets*, *127*(1), e2021JE007118. doi: https://doi.org/10.1029/

2021JE007118

Phillips, C. B., Burr, D. M., & Beyer, R. A. (2007). Mass movement within a slope streak on mars. *Geophysical Research Letters*, *34*(21). Retrieved from `https://agupubs.onlinelibrary.wiley.com/doi/abs/10.1029/2007GL031577` doi: https://doi.org/10.1029/2007GL031577

Posiolova, L. V., Lognonné, P., Banerdt, W. B., Clinton, J., Collins, G. S., Kawamura, T., . . . Zenhäusern, G. (2022). Largest recent impact craters on mars: Orbital imaging and surface seismic co-investigation. *Science*, *378*(6618), 412-417.

Roberts, G. P., Matthews, B., Bristow, C., Guerrieri, L., & Vetterlein, J. (2012, February). Possible evidence of paleomarsquakes from fallen boulder populations, Cerberus Fossae, Mars. *J. Geophys. Res. Planets*, *117*(E2), n/a-n/a. doi: 10.1029/2011JE003816

Rosser, N., Kincey, M., Oven, K., Densmore, A., Robinson, T., Pujara, D. S., . . . Dhital, M. R. (2021). Changing significance of landslide hazard and risk after the 2015 mw 7.8 gorkha, nepal earthquake. *Progress in Disaster Science*, *10*, 100159.

Schorghofer, N., Aharonson, O., Gerstell, M., & Tatsumi, L. (2007). Three decades of slope streak activity on mars. *Icarus*, *191*(1), 132-140. Retrieved from `https://www.sciencedirect.com/science/article/pii/S0019103507001960` doi: https://doi.org/10.1016/j.icarus.2007.04.026

Schorghofer, N., Aharonson, O., & Khatiwala, S. (2002). Slope streaks on Mars: Correlations with surface properties and the potential role of water: Slope streaks on Mars. *Geophysical Research Letters*, *29*(23), 41–1–41–4. Retrieved 2022-07-14, from `http://doi.wiley.com/10.1029/2002GL015889` doi: 10.1029/2002GL015889

Schorghofer, N., & King, C. M. (2011). Sporadic formation of slope streaks on Mars. *Icarus*, *216*(1), 159–168. Retrieved 2022-07-14, from `https://linkinghub.elsevier.com/retrieve/pii/S0019103511003459` doi: 10.1016/j.icarus.2011.08.028

Smith, D. E., Zuber, M. T., Frey, H. V., Garvin, J. B., Head, J. W., Muhleman, D. O., . . . Sun, X. (2001). Mars orbiter laser altimeter: Experiment summary after the first year of global mapping of mars. *Journal of Geophysical Research: Planets*, *106*(E10), 23689-23722.

Stähler, S. C., Mittelholz, A., Perrin, C., Kawamura, T., Kim, D., Knapmeyer, M., . . . Banerdt, W. B. (2022). Tectonics of Cerberus Fossae unveiled by marsquakes. *Nature Astronomy*, *6*(12), 1376–1386. doi: 10.1038/s41550-022-01803-y

Sullivan, R., Thomas, P., Veverka, J., Malin, M., & Edgett, K. S. (2001). Mass movement slope streaks imaged by the mars orbiter camera. *Journal of Geophysical Research: Planets*, *106*(E10), 23607-23633. doi: https://doi.org/10.1029/2000JE001296

Tanaka, K., Skinner, J., Jr., D., J.M., I., Irwin R.P., Kolb, E., Fortezzo, C., . . . Hare, T. (2014). Geologic map of mars. *U.S. Geological Survey Scientific*, *pamphlet 43 p.*. doi: 10.3133/sim3292

Tatard, L. (2010). *Statistical analysis of triggered landslides : implications for earthquake and weather controls* (Unpublished doctoral dissertation). University of Canterbury and Université de Grenoble.

Valantinas, A., Becerra, P., Pommerol, A., Tornabene, L., Affolter, L., Cremonese, G., . . . Thomas, N. (2021). CaSSIS color and multi-angular observations of Martian slope streaks. *Planetary and Space Science*, *209*, 105373. Retrieved 2022-07-14, from `https://linkinghub.elsevier.com/retrieve/pii/S0032063321002129` doi: 10.1016/j.pss.2021.105373

Watters, T. R. (1993). Compressional tectonism on Mars. *Journal of Geophysical Research*, *98*(E9), 17049. Retrieved from `http://doi.wiley.com/10.1029/93JE01138` doi: 10.1029/93JE01138

Wieczorek, M. A., Broquet, A., McLennan, S. M., Rivoldini, A., Golombek, M., Antonangeli, D., . . . Banerdt, W. B. (2022). Insight constraints on the global character of the martian crust. *Journal of Geophysical Research: Planets*, *127*(5), e2022JE007298.